

Development of a hardware-in-the-loop testbed to demonstrate multiple spacecraft operations in proximity

Youngho Eun, Sang-Young Park*, Geuk-Nam Kim

Astrodynamics and Control Laboratory, Department of Astronomy, Yonsei University, Seoul, 03722, Republic of Korea

ARTICLE INFO

Keywords:

Hardware-in-the-loop testbed
Spacecraft proximity operation
Formation flying
Hardware characterization

ABSTRACT

This paper presents a new state-of-the-art ground-based hardware-in-the-loop test facility, which was developed to verify and demonstrate autonomous guidance, navigation, and control algorithms for space proximity operations and formation flying maneuvers. The test facility consists of two complete spaceflight simulators, an aluminum-based operational arena, and a set of infrared motion tracking cameras; thus, the testbed is capable of representing space activities under circumstances prevailing on the ground. The spaceflight simulators have a maximum of five-degree-of-freedom in a quasi-momentum-free environment, which is produced by a set of linear/hemispherical air-bearings and a horizontally leveled operational arena. The tracking system measures the real-time three-dimensional position and attitude to provide state variables to the agents. The design of the testbed is illustrated in detail for every element throughout the paper. The practical hardware characteristics of the active/passive measurement units and internal actuators are identified in detail from various perspectives. These experimental results support the successful development of the entire facility and enable us to implement and verify the spacecraft proximity operation strategy in the near future.

1. Introduction

Space activities occurring in proximity, such as in autonomous rendezvous and docking (ARD), rescue, and other various on-orbiting services, are receiving considerable interest as a result of advances in modern space technology. Furthermore, by utilizing a number of agents in a group, such as in spacecraft formation flying, future space missions are expanding into as yet unexplored applications in astronomy, astrophysics, earth science, heliophysics, etc. [1–5]. These envisioned operational concepts have several advantages compared to traditional single large spacecraft. For example, a higher level of scientific objective can be achieved with a large virtual caliber space telescope, mission endurance and robustness can be assured by replacing malfunctioned agents in the group, and the launch cost can be reduced because of the relatively small mass of individual spacecraft. However, highly complex and challenging scientific objectives enlarge the level of operational difficulty. Therefore, it is necessary to improve an autonomous relative guidance, navigation, and control (GNC) system from a relative point of view to ensure the safety and capability of future space activities. Recent formation flying missions concerning experimental technical demonstrations can be found in Refs. [6–9].

Instead of conducting a costlier in-space demonstration, the hardware-in-the-loop air-bearing testbed enables validation of the GNC

strategies at relatively low cost. Compared to a software-based validation, this method provides adequate fidelity by reproducing the dynamical representative environment and various hardware phenomena. Hence, an end-to-end system-level evaluation experiment can be carried out by reflecting these practical issues as closely as possible. Air-bearing-based vehicles represent a spacecraft in space by operating on a planar surface. This is enabled by the air-bearings located on the vehicle and as long as the surface is horizontally leveled, residual acceleration due to gravity and friction is minimal. Utilizing internal actuators in this quasi-momentum-free environment and an appropriate in-door localization system, orbital spaceflight can be emulated with high reliability. Over the past decade, a number of institutes have developed testbeds with the aim of applying various modern GNC algorithms. For a brief survey of these air-bearing testbeds, the reader is referred to the published work [10,11]. Among the studies conducted in various institutes, we introduced the most advanced testbeds developed in very recent times. NASA Jet Propulsion Laboratory (JPL) developed the Formation Control Testbed (FCT), which consists of two six-degree-of-freedom (6-DOF) robots to demonstrate a formation flying control system for the Terrestrial Planet Finder Interferometer (TPF-I) [12]. The German aerospace center (DLR) constructed the Test Environment for Applications of Multiple Spacecraft (TEAMS) to test GNC formation flying algorithms [13]. The University of Florida developed an

* Corresponding author.

E-mail addresses: yheun@yonsei.ac.kr (Y. Eun), spark624@yonsei.ac.kr (S.-Y. Park).

innovative 6-DOF simulator, the ADvanced Autonomous Multiple Spacecraft (ADAMUS) testbed, without utilizing any servo actuators to manipulate vertical motion [14]. Georgia Tech expanded their pre-developed 3-DOF attitude simulator into the 5-DOF Autonomous Spacecraft Testing of Robotic Operations in Space (ASTROS) testbed [15]. Lastly, the Naval Postgraduate School (NPS) recently developed the Proximity Operation of Spacecraft: Experimental hardware-In-the-loop DYNamic (POSEIDYN) simulator, which is a fourth generation testbed of the institute, to experimentally test algorithms for autonomous rendezvous and proximity operations [16].

In this research, we introduce the Autonomous Spacecraft Test Environment for Rendezvous In proXimity (ASTERIX) facility developed at the Astrodynamics and Control Laboratory (ACL). The new testbed is developed to provide a space-representative environment to experimentally evaluate GNC algorithms for proximity operation and formation flying. Based on the prototypes that were developed in the past few years [17,18], continuous design modifications were made to enhance the structural efficiency and stability. The complete ASTERIX facility consists of two identical 5-DOF spaceflight simulators (for convenience, we henceforth denote this as *simulator*, *vehicle*, or *platform*), an aluminum-covered operational arena, and a surrounding motion capture system. Except for the tracking system, the simulators were designed and built entirely by the ACL. The operational arena was designed by ACL and built by Shinhan A-Tec. A detailed description of each one of the elements is provided in the paper including the main components such as the measurement sensors and internal actuators. In order to quantify the performance and to ensure the operational capabilities of the system, the measurement and actuation system was additionally characterized by conducting an experimental evaluation. The developed testbed is planned not only for the validation of the GNC algorithm but also to realize space mission objectives. This is enabled by leaving the central area of the attitude stage free such that a particular scientific instrument could be accommodated there. Moreover, the main plates of the platform have a wide number of extra tapped holes so that additional equipment, such as cameras and docking port, can be attached in the future. This versatile design is a special feature of the ASTERIX facility and allows a miniaturized version of space activities such as solar alignment and attitude synchronization to be performed [8,9,19,20]. Thus, we can remark that the new facility has advantages in operational expandability compared to the aforementioned facilities. The foremost contribution of this paper can be summarized as:

1. Introduction of the 5-DOF ASTERIX testbed, which emulates multiple spacecraft motions via an equivalent principle of motion. (to the author's knowledge, only NASA JPL has previously developed multiple 5-DOF simulators)
2. Demonstration of the detailed hardware characteristics, which is hard to find in most of the relevant literature, to quantify the capabilities of the testbed to enable a proper comparison to be made among different experimental environments.
3. Development of a versatile testbed to visually reproduce and evaluate scientific space mission objectives under circumstances prevailing on the ground.

The layout of the paper is as follows: First, the hardware architecture of the ASTERIX testbed is described in detail in Section 2 by considering every component. Second, the hardware characteristics of the components, such as the accuracy and noise properties of both the internal and external measurement system, and the capability of internal actuators, are analyzed in Section 3. Lastly, the final section presents the concluding remarks.

2. Testbed description

The ASTERIX facility consists of three main elements. First, the

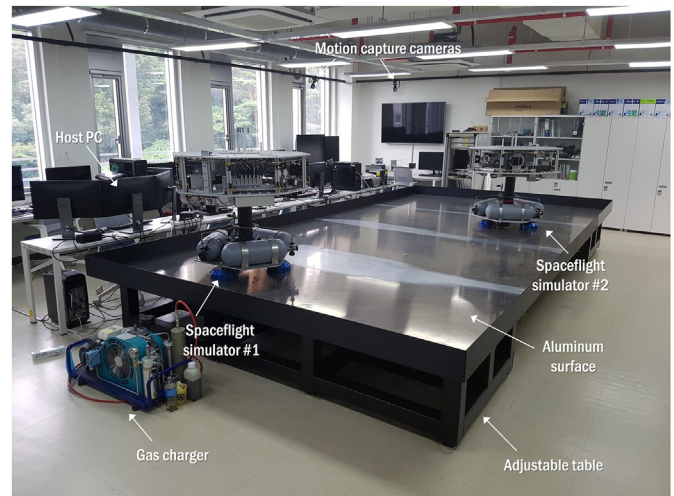


Fig. 1. Overview of the ASTERIX facility.

spaceflight simulator represents a spacecraft agent in space by imitating its principle of motion. Second, the operational arena provides a large flat surface upon which the vehicles can move freely. Lastly, the surrounding tracking system covers the whole facility and traces the real-time position and attitude of the vehicles. All these elements work complementarily to demonstrate spacecraft proximity operations such as formation flying and ARD on the scale of a ground laboratory. The facility is again categorized into a number of subsystems by their functionalities [21]: attitude determination and control subsystem (ADCS), telemetry, tracking, and command (TTNC), command and data handling (CNDH), electrical power subsystem (EPS), guidance and navigation subsystem (GNS), structures and mechanisms subsystem (SMS), and an additional kinematic subsystem (KS) to compromise ground-based factors such as gravity and friction. Unlike real spacecraft operation in space, thermal control issues were not considered because of the absence of a such remarkable heat source inside the laboratory. An overview of the facility including all the elements is shown in Fig. 1.

2.1. Operational arena

The operational arena generates and provides a space-borne environment for the simulators. In other words, it enables the vehicles to move freely without experiencing a major disturbance such as gravity and friction, which are relatively dominant on the ground compared to space. Hence, it is necessary to build a smooth and solid surface to minimize friction and avoid a vortex while operating the linear air-bearings. At the same time, the surface must be leveled with care to prevent natural gravitational drift which is now likely to arise due to the aforementioned low amount of friction. Typically, granite and epoxy are the most popular material used to construct this kind of operational arena [13–16,22]. Among these materials, granite is known to have the most stiffness and can be processed smoothly within only a few microns of flatness. Epoxy is preferred when a wide range of operational arena is needed [11]. However, neither of these materials are compatible with our laboratory conditions. Granite was excluded owing to its considerable weight and epoxy is known to have several undulations during construction and these local gradients even worsen as time proceeds. Therefore, as an alternative to these widely used materials, we decided to cover the surface with a set of aluminum plates as in Ref. [12]. Despite the reduced smoothness of the surface compared to granite, the levitation performance was verified first with the pre-developed prototype [17]. Four 3060 mm × 1580 mm aluminum plates were organized side by side to cover a total of 6320 mm × 3060 mm of the operational arena. Four honeycomb-based tables support these aluminum plates that are manually leveled within a precision of

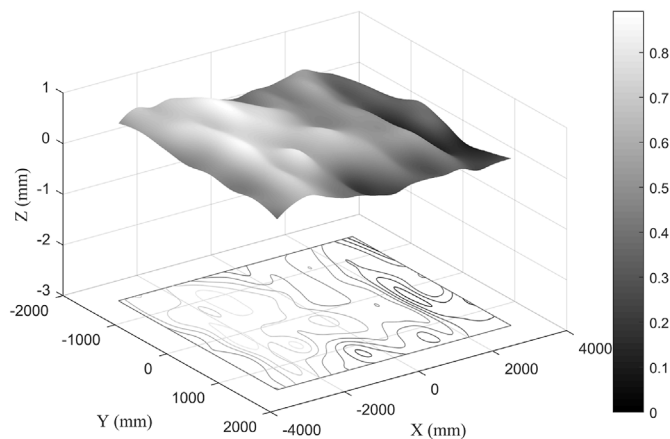


Fig. 2. Height map measurement of the operational arena.

0.01 mm/100 mm. The gap between these plates was filled with dilute epoxy and irregularities at the edges were processed again with an angle grinder. A safety wall was installed at the boundaries of the arena to prevent the vehicles from falling off.

Despite the use of a sufficiently flat and smooth material, construction imperfections, which could cause local residual acceleration of the simulators, still existed. Hence, this would have to be considered as a local perturbation or disturbance to perform an accurate experiment. Fig. 2 shows the overall height map of the operational arena. The measurement was carried out with an SPI TRONIC PRO 3600, which has a resolution of 0.01° with an accuracy of $\pm 0.05^\circ$. The inclination was measured every 400 mm and again interpolated to 10 mm. The maximum local inclination turned out to be -0.07° and the maximum local displacement with respect to the lowest point of the arena is 0.863 mm.

2.2. Tracking system

An OptiTrack motion capture system was installed around the laboratory to cover the full field of view of the operational arena. The tracking system mainly consists of eight Prime 13 cameras shown in Fig. 3a, each with a resolution of 1.3 megapixel, a 240-fps frame rate and three-dimensional measurement precision as fine as 0.5 mm at long range and 0.2 mm in close proximity [23]. Each of the members is supported with power-over-Ethernet (POE) by using one Cisco SG300 hub switch which is directly connected to the tracking computer. Motive, the dedicated software of OptiTrack, continuously provides the real-time three-dimensional position of the reflective markers as shown in Fig. 3b. The observed data is delivered by wireless transmission using a WiFi network with the help of the NatNet SDK protocol. Although this occurs passively in a separate host computer, all broadcasting processes require only a few milliseconds. Further detailed specification of the tracking system is discussed in Section 3.

2.3. Spaceflight simulator

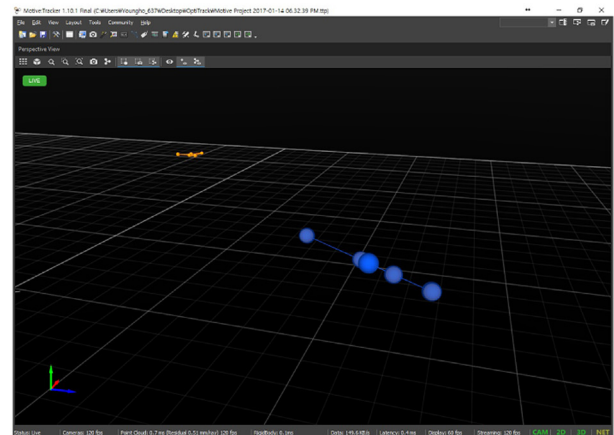
The spaceflight simulator consists of two main structures: translation and attitude stages. The lower translation stage supports the upper attitude stage and provides a maximum of 5-DOF to the total platform: two DOF for full planar motion and three DOF for limited rotational motion. The mounted attitude stage emulates a spacecraft by measuring and manipulating its position and attitude by itself. The complete configuration of the simulator is shown in Fig. 4.

2.3.1. Translation stage

The kinematic subsystem employs one hemispherical with a radius of 63.5 mm and a set of three linear air-bearings with a diameter of 200 mm with a supporting pneumatic system. While the linear air-



(a) OptiTrack Prime 13 camera



(b) Motive tracking reflective markers

Fig. 3. Tracking system.

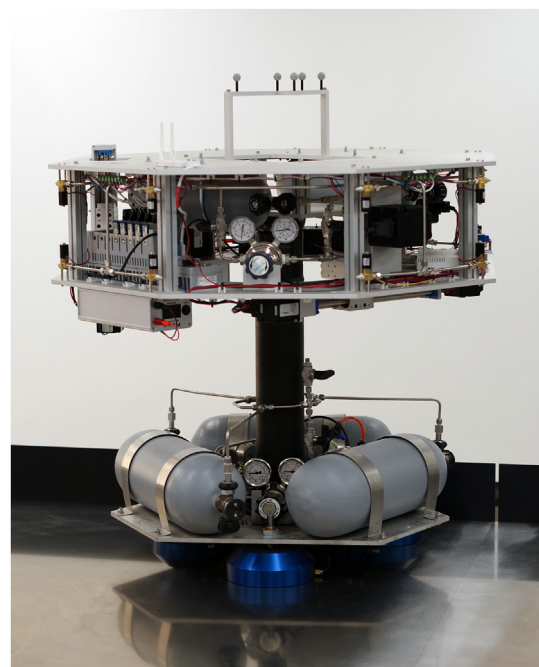
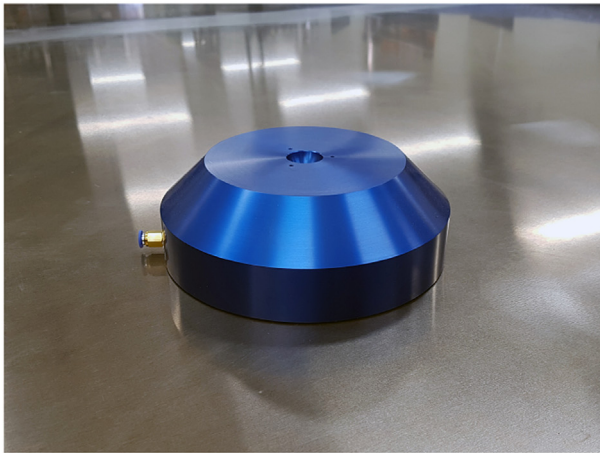


Fig. 4. Spaceflight simulator.



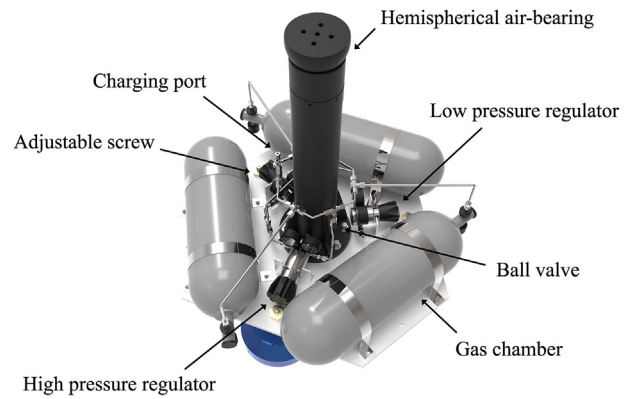
(a) Linear air-bearing



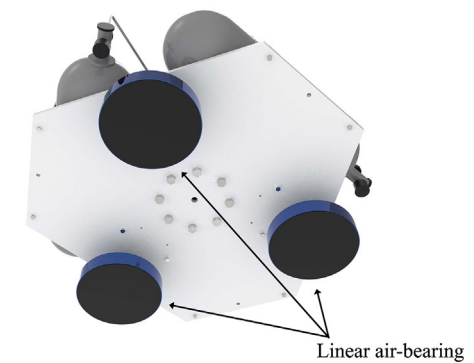
(b) Hemispherical air-bearing

Fig. 5. Air-bearings before installation.

bearings generate a film of thin air of $5\ \mu\text{m}$ on the operational surface, the hemispherical air-bearing achieves this between two stages to enable frictionless rotational motion. Whereas the inclination of the roll and pitch motion is limited up to 45° , the yaw motion is unbounded around the axis perpendicular to the ground. Fig. 5 shows each of the air-bearings before attachment to the simulator. Fig. 6 shows the



(a) Upper view



(b) Lower view

Fig. 7. Components of translation stage.

pressure regulation strategy of the translation stage. With the three 9 L gas chambers charged up to 30 MPa, a two-step pressure regulation strategy is used to precisely adjust and supply compressed gas to the working level. The operating pressure is set to be 0.5 MPa for all air-bearings and each of the sets is activated manually with hand valves. Because of the high initial pressure, the gas chambers are connected to each of the regulators via a stainless steel pipe with a diameter of 6.25 mm and thickness of 1.57 mm. The remaining routing for air-bearings is carried out with polyurethane tubes. The supporting structure including the main plate and pedestal is designed and produced of

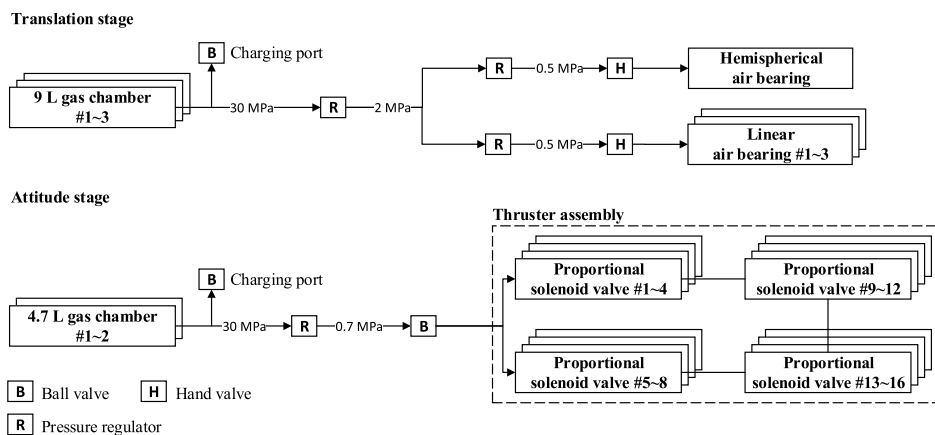
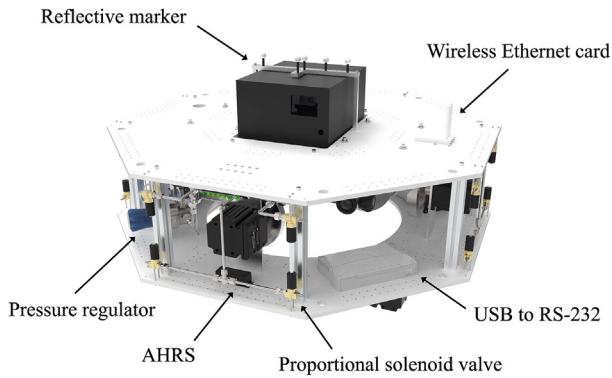


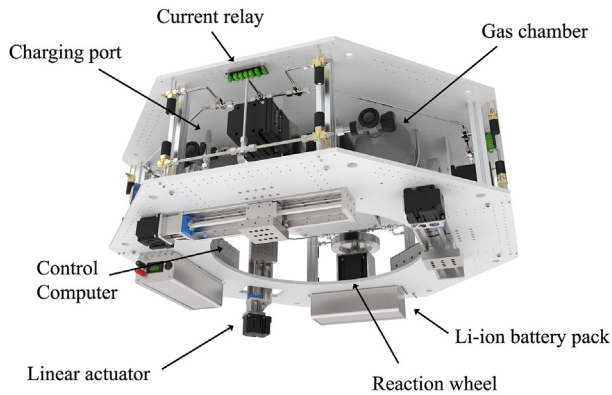
Fig. 6. Pneumatic system of spaceflight simulator.

Table 1
Components of translation stage.

Component	Model	Amount	Remarks
Gas chamber	SCA790	3	9 L, 30 MPa
High-pressure regulator	44-116124	1	30 MPa → 2 MPa
Low-pressure regulator	44-2263241	2	2 Mpa → 0.5 Mpa
Linear air-bearing	S1020001	3	–
Hemispherical air-bearing	SRA250-R45	1	45° tiltable
2-way ball valve	VH86B-D-4T-PK-S	2	–
2-way hand valve	HVFF 06-06	2	–
Structure	Custom (AL6061)	1	–



(a) Upper view



(b) Lower view

Fig. 8. Components of attitude stage.

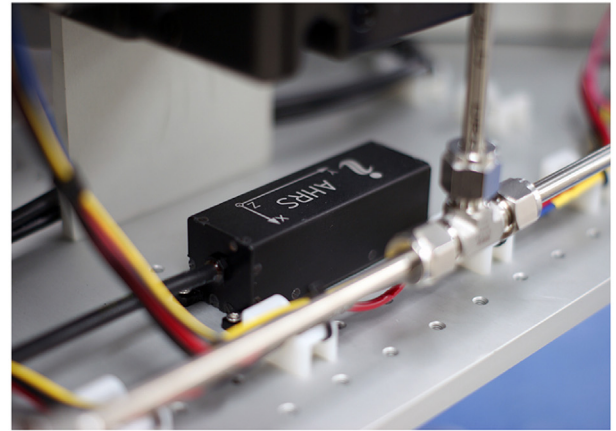
aluminum alloy 6061. The total height of the translation stage is approximately 820 mm and the longest diagonal of the main plate is 800 mm. Finally, the mass of the translation stage is approximately 59.47 kg. Fig. 7 and Table 1 show detailed information of every component of the translation stage.

2.3.2. Attitude stage

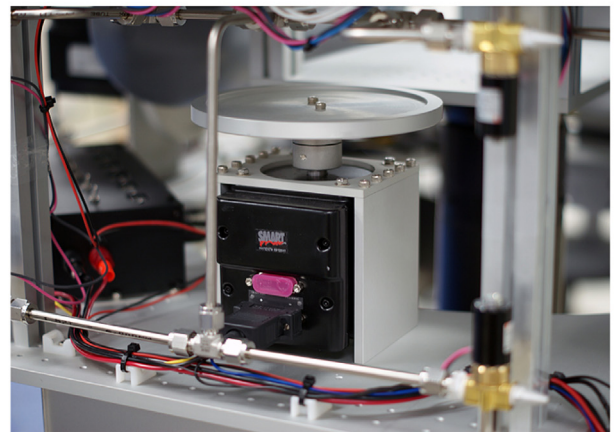
Fig. 8 and Table 2 show the design and configuration of the components on the attitude stage. This stage carries all the remaining equipment for operation and, with the help of the translation stage, emulates the motion of a spacecraft in space. The attitude stage is again divided into three stages based on their positions. The lower stage contains most of the components such as the reaction wheel assembly (RWA), control computer, gas regulator, battery packs, and automatic mass balancing system. The upper stage carries the gas chambers and reflective markers. Lastly, the middle stage provides space for a payload, such as a laser distance meter and vision-based camera, for future utilization.

Table 2
Components of attitude stage.

Component	Model	Amount	Remarks
Attitude sensor	AHRS-G1000-TMGA-C1-V1.1	1	–
Reaction wheel	SM34165DT-CDS	3	max 5100 RPM
Reflective marker	MKR190M4	5	–
Wireless Ethernet	A2000UA	1	–
Control computer	NI cDAQ-9139	1	1.33 GHz, 2 GB RAM
Analog voltage input	NI 9221	1	–60~60 V × 8 ch
Analog current output	NI 9265	4	0~20 mA × 4 ch
Serial interface	NI USB-232/4	1	–
Li-ion battery pack	Custom	2	–
DC-DC converter	SZH-PWSD-011	5	–
Proportional solenoid valve	PVQ31-5G-16-01-F-X33	16	0~100 LPM
High-pressure regulator	SG3-63150	1	30 MPa → 0.7 MPa
2-way ball valve	VH86B-D-4T-PK-S	2	–
Gas chamber	SCA420	2	4.7 L, 30 MPa
Linear actuator	L1-0250/0200-050R-AN	3	5 mm/rev
Servo motor	SM23165DT-CDS	3	–
Structure	Custom (AL6061)	1	–



(a) Attitude and heading reference system



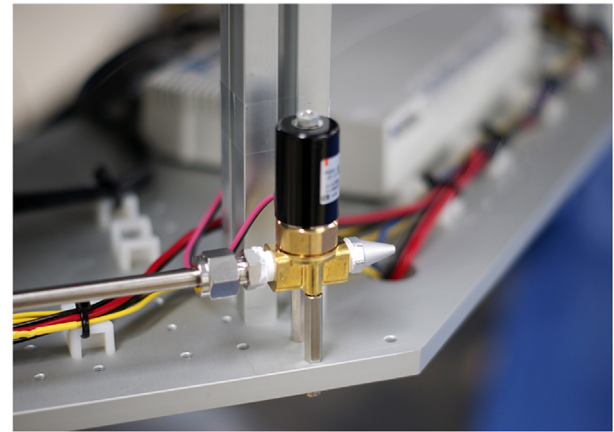
(b) Reaction wheel

Fig. 9. Attitude determination and control subsystem.

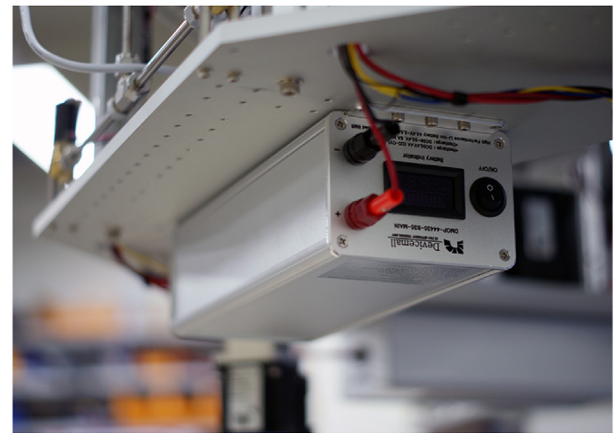
The ADCS is realized with an attitude and heading reference system (AHRS) and a set of RWA, which are shown in Fig. 9. The AHRS measures the orientation angle of simulators with a combination of

instruments consisting of a magnetometer, accelerometer, and gyro. The magnetometer is used to determine the initial heading (yaw) angle and to correct gyro drifts in the heading angle determination, whereas the accelerometer completed the task for the tilt (roll, pitch) angles. A built-in robust Kalman filter estimates the gyro bias drift and calculates the stabilized orientation angles. Precisely aligned to the vehicle body frame, the AHRS measures angular displacement with an accuracy of 0.7° for the heading and 0.3° for the tilt angles. The accuracy of the scale factor of the rate of change is 0.1%. Each orientation angle and rate has a resolution of 0.01° and $0.01^\circ/\text{s}$, respectively. The update rate is up to 100 Hz, every data set can be achieved by transmitting a set of hexadecimal commands through serial communication. The RWA consists of three components: the Animatics SmartMotor, flywheel, and coupler. The SmartMotor is an integrated system that contains a servo motor, encoder, amplifier, controller, and RS-232 communication in a single unit to reduce the configuration complexity. The maximum torque is known to be 3.39 N m and the rotation speed is 5100 RPM with no load. The flywheel is designed and produced from aluminum alloy 6061 with a diameter of 160 mm and mass of 0.422 kg. The moment of inertia for the rotational axis is $1.5309 \times 10^{-3} \text{ kg}\cdot\text{m}^2$ based on the CAD model. Therefore, considering the aforementioned specification, each reaction wheel is capable of carrying an angular momentum of up to approximately $0.8176 \text{ kgm}^2/\text{s}$. A detailed explanation of the selection of the flywheel size and inertia is provided in Section 3. The coupler connects the motor and flywheel by tightening their shafts together. Three linear actuators are installed to configure the automatic mass balancing system. Each of the actuators is aligned to the body frame and a small mass is attached to the carrier. Since the rotational motion of the attitude stage is strictly bounded to that of the motion of the hemispherical air-bearing, which is attached to the bottom of the middle stage, every time torque is applied to the attitude stage it acts on a fixed point on the air-bearing. Therefore, this center of rotation (CR) necessitates additional consideration while the vehicles are rotating. In our case, the centroid of the hemispherical air-bearing is regarded as the CR of the entire attitude stage. If the center of mass (CM) of the attitude stage does not coincide with the CR, natural rotational motion is generated as a result of gravity; thus, the attitude stage surely oscillates in a way similar to a pendulum until the vector from CR to CM is aligned towards the center of Earth. Hence, the first priority is to match the CM with the CR precisely by moving the loaded mass. However, since it is very difficult to match both points perfectly in practice, the next priority is to locate the CM strictly below the CR to avoid unstable motion.

The PS consists of a thruster assembly and supporting pneumatic system. The thruster assembly is again composed of 16 proportional solenoid valves and custom-made nozzles as shown in Fig. 10a. These thrusters are used to generate force and torque for both the translational and rotational motion. By utilizing proportional solenoid valves, variable thrust is imitated by adjusting the input current of 8~20 mA to control the flow rate within a range of 0~100 L/min. As shown in Fig. 8, the thrusters are located symmetrically with respect to the CR. Therefore, each thruster can be controlled individually such that the net thrust corresponds to the CR when only translational motion is needed. On the other hand, if rotational motion torque is needed, control torque can be generated by actuating the thrusters at the symmetrical point. Fig. 6 shows the gas distribution strategy of the attitude stage. Two 4.7 L gas chambers support the entire thruster assembly by charging up to 30 MPa of gas. Similar to the pneumatic system of the translational stage, the charged gas at 30 MPa is dropped to the operational pressure of 0.7 MPa by a single gas regulator. Here, the pressure regulator in the attitude stage has high flow capacity relative to that of the translational stage to fulfill the relatively high flow demand. The location of the chambers is determined such that their CM is strictly above that of CR even if the internal gas is completely consumed. This guarantees that the attitude stage is structurally robust by preventing the aforementioned instability such as inverted pendulum motion that could occur if



(a) Thruster assembly



(b) Custom battery pack

Fig. 10. Thruster and Li-ion battery pack.

the chambers are located beneath the CR. Unlike that of the translational stage, the entire PS subsystem, the chambers, regulator, and thrusters are connected with a stainless steel pipe to prevent possible mass disorder that would result from using a flexible tube. Two ball valves are utilized for activating the thrusters and charging gas chambers, respectively.

Fig. 11 shows the command and measurement flow of all the electronic devices on the attitude stage and their power supply strategy. Four digital to analog converter (DAC) modules generate control current for the entire thruster assembly, one analog to digital converter (ADC) module monitors every voltage supplied by the Li-ion battery pack and the DC-DC converters. One USB to RS-232 converter connects the AHRS, RWA, and automatic mass balancing system with the control computer. As mentioned above, the AHRS transmits the current orientation angle and rate in response to the user's request. Similarly, the RWA is controlled by a user command written in the ASCII character set and is also capable of transferring the current rotation speed by utilizing the internal encoder. The command for the automatic mass balancing system is identical to that of RWA, which in this case involves adding the position of the carrier to the data set. Unlike a typical RS-232 connection, the RWA and automatic mass balancing system are all connected together with a daisy-chain connection over a single RS-232 port. It is necessary to pre-address these motors individually with a unique number to ensure that all motors are connected in one communication. Wireless Ethernet is connected with USB. Two custom-made Li-ion battery packs shown in Fig. 10b provide voltage up to 48 V with a power capacity of 310 Wh. DC-DC converters are utilized to

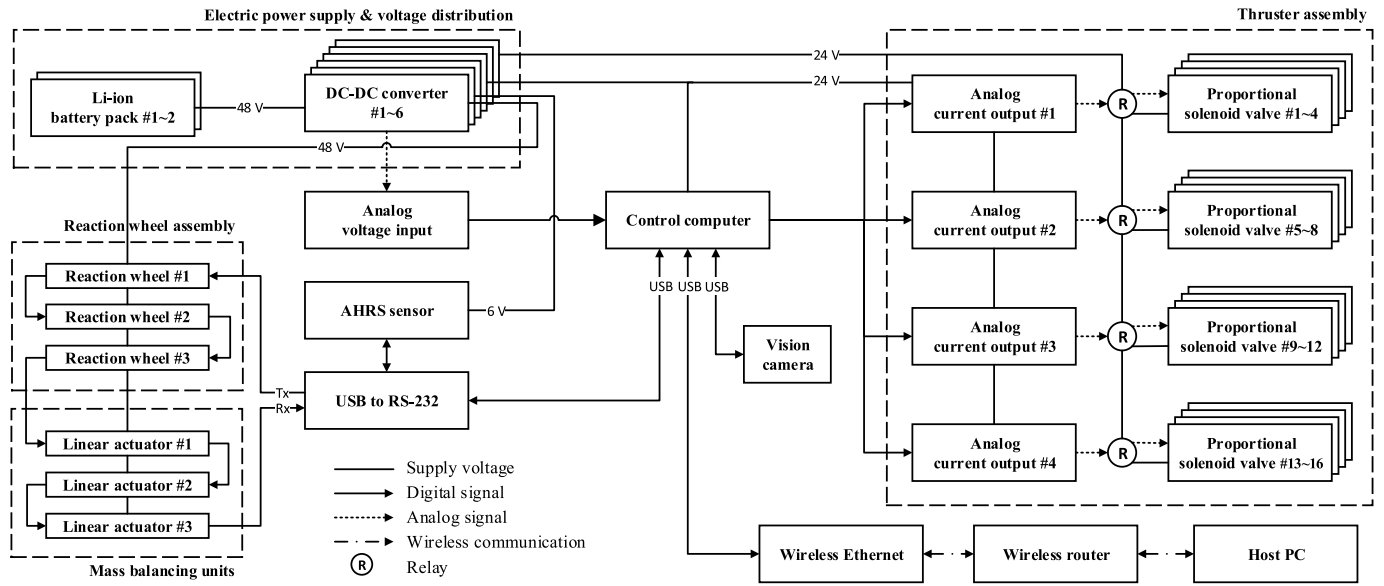


Fig. 11. Command and measurement flow and electric power supply of attitude stage.

adjust the voltage supply with respect to the operational level of each electrical component. For protection purposes, the voltage supply of each device is controlled by a manual switch and monitored individually through both an LED voltage meter and an analog input ADC module. Data communication between simulators and users occurs via wireless Ethernet. First, the real-time position is achieved by the tracking system and based thereupon the desired trajectory is calculated by the host computer. The present and desired positions are continuously streamed into a local network environment provided by a wireless router. Each of the control computers on the simulators receives these data at each time step by request and generates control thrust and torque for operation. Furthermore, the simulators are capable of exchanging their position and attitude information with each other, and users can also receive this consistently. However, even if this process is continuously running in the background, not exactly all of the data are transferred to the receivers due to a small amount of execution time. Latency of several milliseconds is measured on average while transferring and receiving a set of data. The operational environment is organized with Windows/MATLAB for both simulators and users.

Five reflective markers are installed at the top of the attitude stage. To avoid singularity while determining their attitude, the markers are located asymmetrically. The entire supporting structure is designed and produced from aluminum alloy 6061, the total mass of the attitude stage is 87.75 kg, which results in a total of 147.22 kg for the entire platform. Eq. (1) shows the moment of inertia of the attitude stage at the CR with respect to the body frame based on the CAD model. The octahedral plates used in the lower and upper stages have a diameter of 1000 mm and the distance between them is 250 mm. The position of the middle stage is determined such that the CR is located midway between the upper and lower stages. Each of the stages is connected with a 30 × 30 mm aluminum profile. The total height of the entire platform measured from the bottom of the linear air-bearing to the top of the upper stage is 948 mm.

$$I_E = \begin{pmatrix} I_{xx} & I_{xy} & I_{xz} \\ I_{yx} & I_{yy} & I_{yz} \\ I_{zx} & I_{zy} & I_{zz} \end{pmatrix} = \begin{pmatrix} 7.2002 & -0.0882 & -0.1230 \\ -0.0882 & 7.0141 & 0.0493 \\ -0.1230 & 0.0493 & 11.8319 \end{pmatrix} \text{kg} \cdot \text{m}^2 \quad (1)$$

3. System characteristics

This section illustrates and analyzes the components of the facility in detail to quantify and estimate their hardware characteristics. First,

the measurement characteristics of the tracking system and AHRS are identified. Next, the performance of the internal actuators such as the thrusters and reaction wheel assemblies is analyzed.

3.1. Measurement system

3.1.1. Motion capture system

As mentioned in Section 2, the absolute three-dimensional position of vehicles are provided by the tracking system. The system consists of a set of cameras, a hub switch, and a tracking computer. The basic flow of observation is as follows: First, the infrared cameras identify every individual marker inside their field of view in combination. Next, the hub switch collects and transfers this marker information to the tracking computer. The dedicated OptiTrack Motive software installed in the host PC calculates the three-dimensional position of each of the individual markers. Here, the positions are provided with respect to a coordinate system of which the origin is fixed on the center of the operational surface. The marker information is again imported into the MATLAB environment with the help of the NatNet SDK protocol. Finally, with the known relative position of each marker inside the rigid body set, we can finally localize the three-dimensional position and attitude of the vehicles.

The hardware characteristics of the tracking system are analyzed in two quantities: measurement interval and accuracy. First, 10,000 dynamic measurements are collected over the operational arena using a calibration wand CWM-250, a Micron series of OptiTrack. The measurement interval is defined as the time consumption while one orientation is calculated throughout the aforementioned procedure. As shown in Fig. 12, the average interval was 8.3371 ms for the total collection and a general normal distribution is observed with a standard deviation of 1.0792 ms. Next, the accuracy and noise characteristics of the tracking system are identified using the same data set. Since the calibration wand used in this experiment is machined out to be extremely precise and labeled to have a width of 250.014 mm, we compared this value with our measurement. According to the manufacturer, the system provides sub-20 μm of accuracy in optimal conditions [23]. As shown in Fig. 13, the average width was 249.9943 mm with a standard deviation of 0.2950 mm. Consequently, the overall measurement error with respect to the width of the calibration wand is −19.7499 μm, which satisfies the aforementioned level of accuracy. Therefore, this sub-20 μm positional accuracy can be considered to be sufficient for our purpose and furthermore, attitude information can

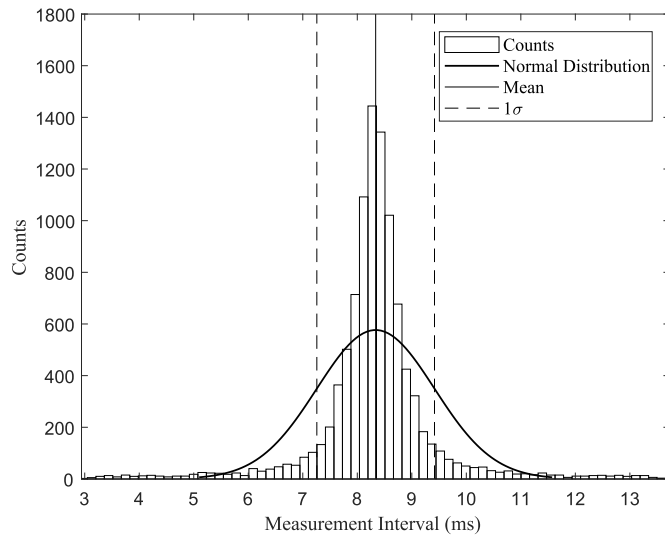


Fig. 12. Measurement interval of tracking system.

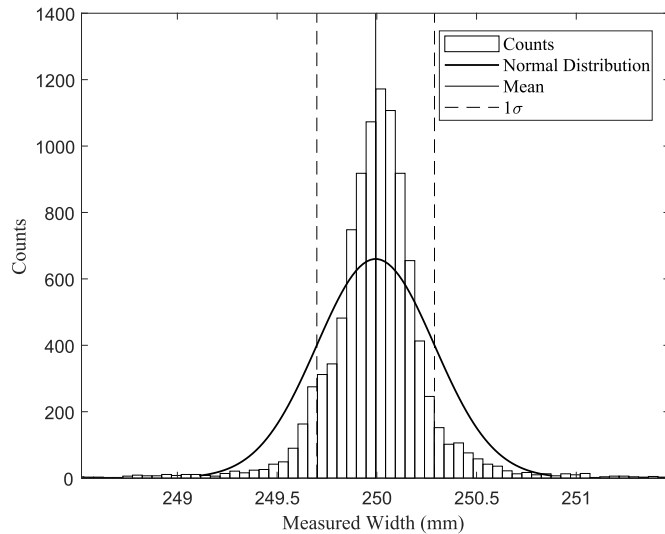


Fig. 13. Reference width measurement of tracking system.

also be provided in precision.

3.1.2. AHRS

Precise three-dimensional attitude information is essential to operate multiple spacecraft in formation. Since ASTERIX aims to demonstrate proximity maneuvers such as alignment and synchronization, active measurement of the simulator orientations is necessary. Although the tracking system is capable of providing accurate attitude orientations, it is appropriate to carry an additional angular measurement device since the tracking is held passively and is meant to replace the GPS signal in principle. Therefore, the attitude of simulators is mainly determined by each AHRS and the tracking system is used to support this measurement. The Inertial Labs AHRS utilizes three-axes accelerometers, magnetometers, and gyroscopes to provide stabilized three-dimensional attitude information for both static and dynamic motion with high precision. Unlike a typical attitude measurement device such as inertial measurement units (IMU), the AHRS provides the absolute orientation of the mounted carrier by utilizing the aforementioned various sensors. A built-in algorithm based on a robust Kalman filter is utilized to determine the initial conditions and to compute the corrected signals for numerical integration. Accelerometers are used to determine the initial tilt alignments and to

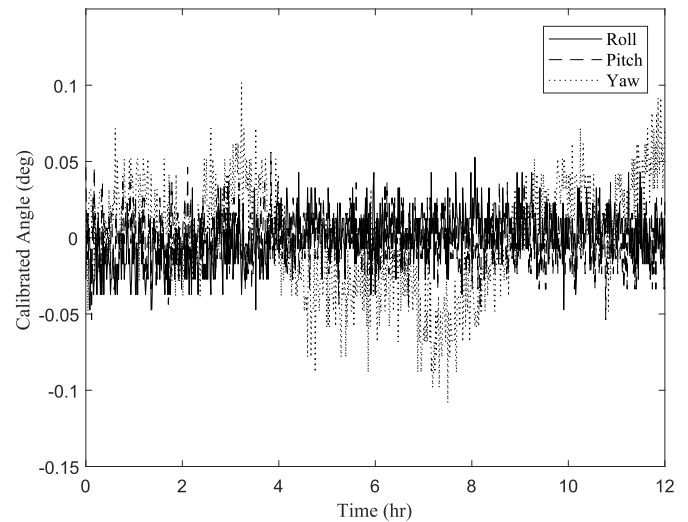


Fig. 14. Static attitude collection of AHRS.

correct the gyro drifts in the determination of the tilt angles. At the same time, fluxgate magnetometers are used to determine the initial heading angle and to correct the gyro drift in the heading angle determination. This ongoing correction of gyro drifts is conducted consistently during operation. The provided orientations (roll, pitch, and magnetic azimuth) are defined on a local coordinate system East-North-Up (ENU) within a sufficient range of measurement.

The noise characteristics of the AHRS were identified by collecting 1,780,122 samples of static measurement data over 12 h with an average sampling interval of 24.2680 ms. Since it is difficult to specify the absolute initial alignment of the simulator in the operational arena, each orientation is calibrated to have a zero mean. As illustrated in Fig. 14, the roll and pitch angle were maintained in the region of $\pm 0.05^\circ$ for the entire time span, whereas the heading (yaw) angle varied slowly in a bound of $\pm 0.1^\circ$. Note that Fig. 14 is drawn with intervals of 2137 to clearly distinguish each signal. Next, the Allan variance method was applied to the entire data set to quantify the magnitude of noise components. As shown in Fig. 15, from the Allan deviation with respect to the averaging time, we can extract some important quantities such as the angle random walk and bias instability. These collected noise properties are compared with the datasheet and summarized in Table 3.

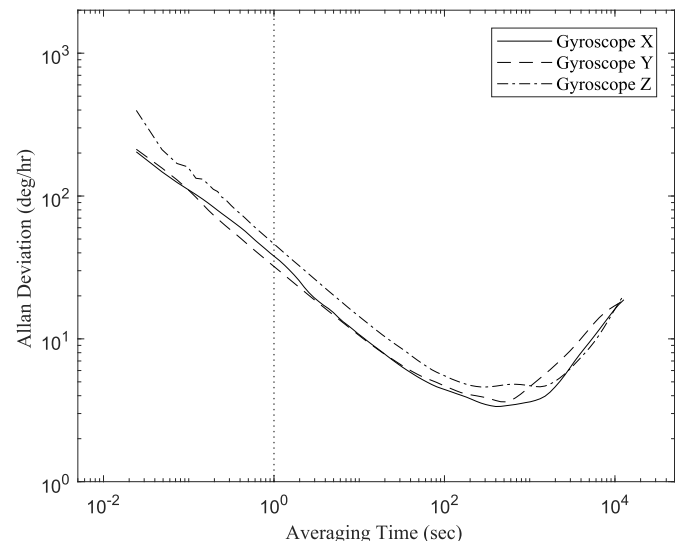


Fig. 15. Gyro Allan variance of AHRS.

Table 3
Static noise characteristics of AHRS.

Parameter	Datasheet	Measurement	Unit
Attitude (roll)	0.02	0.0175	deg RMS
Attitude (pitch)	0.02	0.0170	deg RMS
Heading (yaw)	0.03	0.0347	deg RMS
Bias in-run stability	4	3.8947	deg/hr
Angle random walk	0.009	0.0111	deg/s \sqrt{Hz}

3.2. Internal actuators

3.2.1. Reaction wheel assembly

The hemispherical air-bearing enables frictionless rotation motion to the attitude stage. In this momentum conserved dynamic environment, the angular motion of spacecraft can be represented by actuating the reaction wheels. Even though the thrusters are capable of producing rotational motion, the reaction wheels are considered first. Therefore, the reaction wheels are characterized to determine the rotational performance of the simulators. First, the speed response of unloaded motors with respect to an input command is analyzed. Second, by attaching various flywheels, the change of speed and peak torque with respect to the rotating speed is analyzed to determine the final version of the flywheel. The motor used in this research, an Animatics SM34165DT, is controlled by a range of integers from 0 to 32,767 and negative to the opposite direction. First, the unloaded speed of each motor is measured. An increasing step function from 5000 to the maximum value 32,767 is applied in intervals of 10 s. The rotor speed is measured by an integrated encoder, which can count 1/8000 of a single revolution. The inertia of the rotor itself is $1.0310 \times 10^{-4} \text{ kgm}^2$. As shown in Fig. 16, the speed of rotation proportionally increases with respect to the commanded signal. The error bars reflect 3σ of each measurement period, and the maximum difference of the average magnitude of each measurement samples was 1.7368%. Next, three versions of flywheel are attached to the rotor to evaluate the extent to which the load inertia affects the rotational speed. Since the flywheels and corresponding couplers are produced from solid aluminum alloy and processed precisely, the inertia property is considered to be credible in this work. Hence, the moment of inertia of flywheels is set to be $1.5309 \times 10^{-3} \text{ kgm}^2$, $1.8265 \times 10^{-3} \text{ kgm}^2$, and $3.1837 \times 10^{-3} \text{ kgm}^2$, respectively, throughout the analysis. The inertia of the coupler is $8.2678 \times 10^{-6} \text{ kgm}^2$. As shown in Fig. 17, the average rotational speed with respect to the command signal showed a similar tendency. However, a remarkable spread of the distribution of the rotational speed is

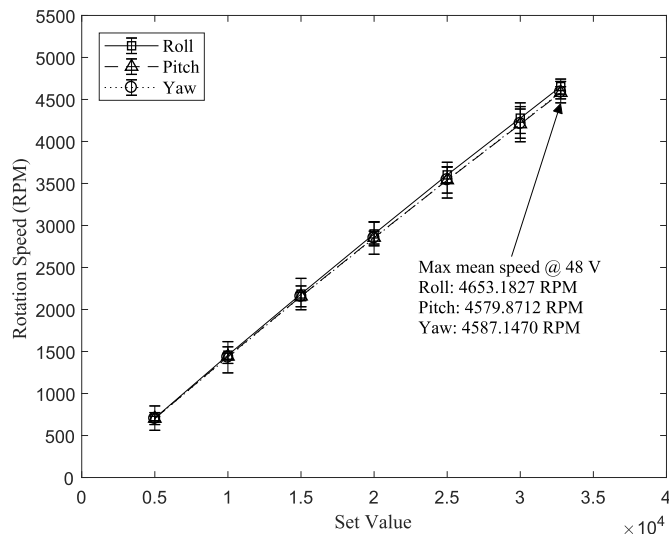


Fig. 16. Speed profile of reaction wheels without load.

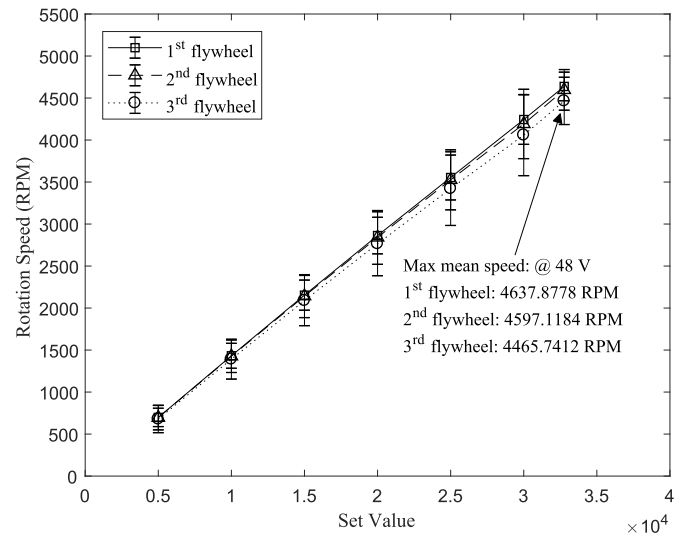


Fig. 17. Speed profile of reaction wheel (yaw) w.r.t. flywheels.

captured compared to the unloaded case. Since each of the flywheels showed similar speed characteristics while having a different moment of inertia, the third version is likely to be selected to operate with maximum angular momentum. However, in the sense of torque production with respect to the rotating speed, as shown in Fig. 18, the overall performance of the first flywheel had superior operation characteristics compared to the others. In other words, it responded quickly to the command; hence, it is capable of transferring the momentum immediately to the platform. The resulting overall characteristics of the reaction wheel with respect to each flywheel are organized in Table 4.

3.2.2. Thruster assembly

Sixteen thruster assemblies are symmetrically arranged with respect to the CR. Each set of four thrusters is set to expel exhaust gas in a fixed direction of the body frame, $\pm x_b$ and $\pm y_b$. Therefore, depending on their location and individual thrust magnitude, the net thrust could drift apart from CR so that unintended rotation takes place when only translational motion is needed. Thruster assembly characterization occurs from three perspectives: First, the output reactivity with respect to various supply pressures is confirmed by applying constantly increasing input commands. Second, the maximum flow magnitude with identical supply pressure is identified to characterize the individual thrust

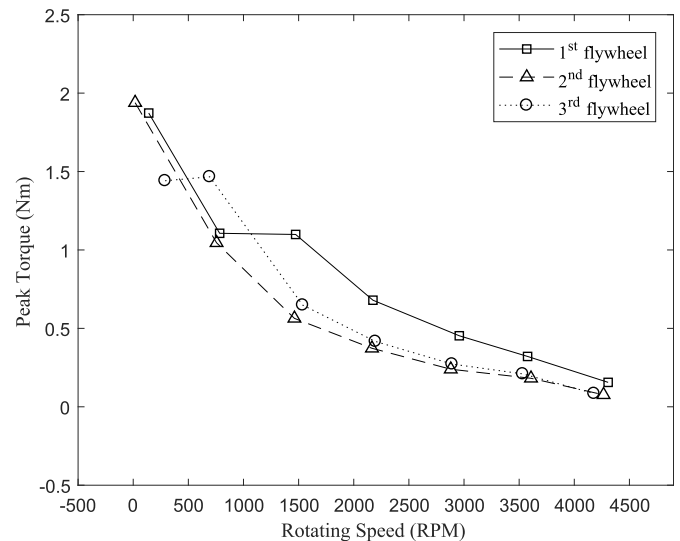


Fig. 18. Peak torque w.r.t. flywheels.

Table 4
Characteristics of reaction wheel w.r.t. flywheels.

Parameter	1st flywheel	2nd flywheel	3rd flywheel	Unit
Total load inertia	1.6395×10^{-3}	1.9351×10^{-3}	3.2923×10^{-3}	kgm^2
Rotating mass	0.478	0.904	1.190	kg
Diameter	160	160	190	mm
Max mean speed	4637.8778	4597.1184	4465.7412	RPM
Max angular momentum	0.7963	0.9316	1.5396	kgm^2/s
Peak torque (@ rest)	1.8729	1.9391	1.4412	Nm

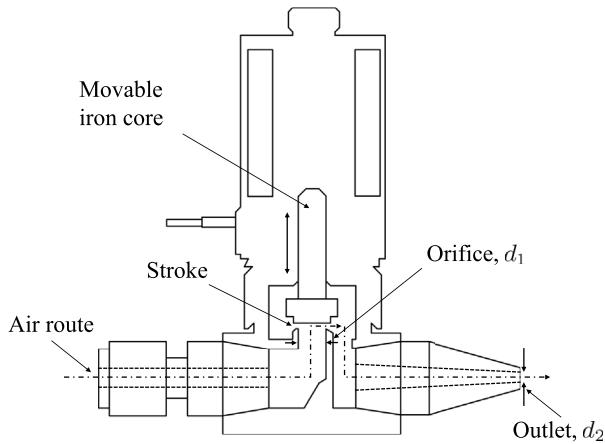


Fig. 19. Schematic views of proportional solenoid valve and nozzle outlet.

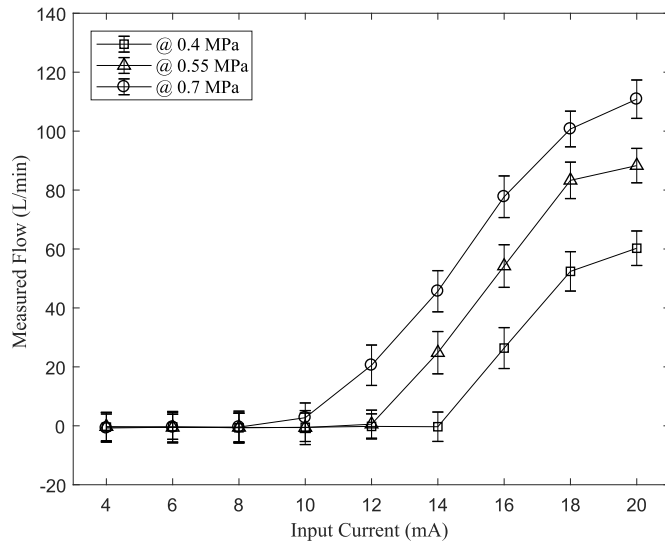


Fig. 20. Flow rate profile of thruster #1.

separately. Lastly, the thrust and the specific impulse of the propulsion system is identified based on the experimental results. As shown in Fig. 19, the proportional solenoid used in this study is capable of lifting the iron core such that the stroke is elevated. Since the height of elevation occurs in response to the applied current, the amount of air through the orifice can be controlled directly by a user command. The nozzle outlet is designed to have the same diameter as the orifice, which is $d_1 = d_2 = 1.6$ mm. As mentioned above, the output response profile is collected at three different supply pressures, 0.4, 0.55, and 0.7 MPa, respectively. The measurement is recorded every 10 s by a digital flow switch SMC PFMB-7201, which can measure up to 200 L/min with an accuracy of $\pm 3\%$ and $\pm 2\%$ of repeatability at full scale. As shown in Fig. 20, a similar tendency appeared throughout the experiment with respect to the constant input range of 4–20 mA. Except for the different

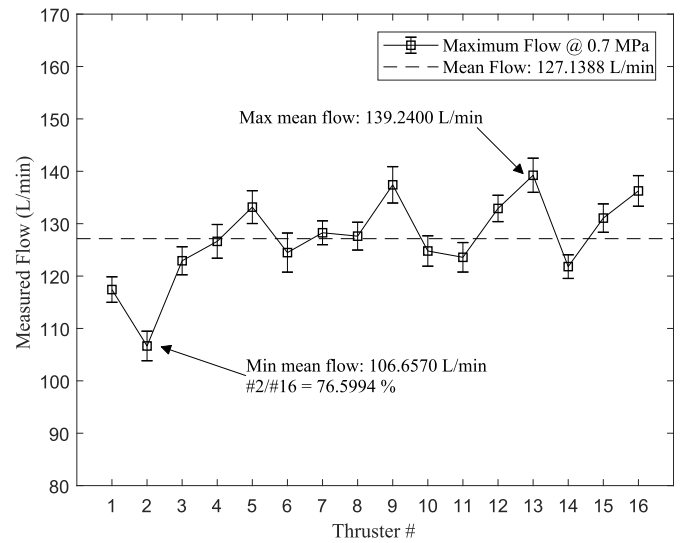


Fig. 21. Flow rate of individual thrusters.

critical points at which the thrust is initially detected, all profiles showed quasi-linear relationships with respect to the input current. Since the solenoid is designed to produce 100 L/min with 0.7 MPa, an average maximum flow approximating 110 L/min is considered to be appropriate. The error bars in Fig. 20 indicates 3σ of each measurement.

The next experiment is carried out to characterize the magnitude of individual thrust. Maximum current is applied for 10 s with 0.7 MPa of supply pressure. As shown in Fig. 21, the inequality of thrust magnitudes is captured. The error bars indicate 1σ of each measurement. The maximum thrust appeared at thruster #13 with a mean value of 139.2400 L/min and minimum at #2 with 106.6570 L/min, which means the minimum ratio of the mean flow, is 76.5994%. In other words, the thrust output of the simulator varies from approximately 83.8902 to 109.5181% among every element with respect to the average thrust. To confirm this result, an additional experiment is performed repeatedly for a single thruster. As shown in Table 5, the average flow \bar{F} seems to be stable for every trial. The overall repeatability was $\pm 1.9866\%$ for thruster #1. Since the repeatability of thrusters δ_F is less than $\pm 3\%$ according to the datasheet, this result is considered to be reasonable. Moreover, from the point of view of the relatively large standard deviation with zero current σ_{F0} , we can conclude that most of the variance in the measurement σ_F is caused by the measurement noise in the flow meter.

Finally, thrust characterization is carried out according to the well-known thrust equation for nozzle jet in Eq. (2):

$$F = \dot{m}v_e$$

$$I_s = v_e/g_0 \quad (2)$$

where F is the thrust, \dot{m} and v_e each denotes the mass flow rate and exhaust velocity, respectively. The specific impulse I_s is a result of the exhaust velocity division standard gravity $g_0 = 9.8067 \text{ km/s}^2$. In this

Table 5
Characteristics of thruster #1.

Trial	Min. F (L/min)	\bar{F} (L/min)	Max. F (L/min)	σ_F (L/min)	σ_{F0} (L/min)	δ_F ($\pm\%$ F.S.)
1	110.6816	117.4264	129.0029	2.4383	2.5415	1.8287
2	108.6192	114.3446	125.4137	2.7632	1.9525	2.0724
3	98.3987	115.3197	124.3539	2.6779	2.6664	2.0084
4	108.9809	117.4564	128.8290	2.8407	1.3731	2.1306
5	111.1219	118.6488	129.4432	2.5237	1.9089	1.8928
Mean	107.5604	116.6392	127.4085	2.6488	2.0885	1.9866

Table 6
Summary of thruster characteristics.

Parameter	Value	Unit
Operation pressure, P	0.7	MPa
Thrust, T	1.2649 ± 0.2446	N
Mass flow rate, \dot{m}	25.0866 ± 4.8507	10^{-4} kg/s
Specific impulse, I_s	51.4136	s

work, we follow the simplified exhaust velocity in Eq. (3) which assumes an isentropic gas flow through a nozzle [24].

$$v_e = \sqrt{\frac{2\gamma}{\gamma-1}RT \left[1 - \frac{P_e}{P} \right]} \quad (3)$$

In the upper equation, γ , R , T , P_e , and P each denotes the isentropic expansion factor, specific gas constant, temperature, pressure at nozzle exit, and supply pressure, respectively. By utilizing the flow measurement results and the density of dry air at standard condition 25°C, the mass flow rate \dot{m} can be calculated. Therefore, we can finally calculate the thrust force of individual thrusters. Table 6 summarizes the characteristics of the thruster assembly along with the average thrust performance and specific impulse.

4. Conclusion

A new ground-based spacecraft test facility developed at the Astrodynamics and Control Laboratory is introduced. Among the existing testbeds around the world, the facility has differentiated utilities for demonstrating various space operations. The facility will be utilized to reproduce space activities by not only verifying the guidance, navigation, and control system but also visualizing various scientific mission objectives under laboratory conditions. Every constitute of the testbed is categorized into several components and again organized into a number of subsystems by their functionality. The description and design procedure of each of the components and subsystems are addressed in detail as much as possible throughout the work. Lastly, the characteristics of the measurement systems and the internal actuators are driven by experiments to specify and quantify the capabilities of the testbed. Most of the components showed satisfactory outcome with respect to the hardware specifications; however, the variance in the individual thrust magnitude indicates the necessity of the implementation of robust or adaptive control techniques. In future we plan to include the practical application of relative guidance, navigation, and control algorithms and focus on the demonstration of space activities.

Acknowledgments

This work was supported by Global Surveillance Research Center (GSRC) program funded by the Defense Acquisition Program

Administration and Agency for Defense Development.

References

- [1] K. Danzmann, Lisa mission overview, *Adv. Space Res.* 25 (6) (2000) 1129–1136.
- [2] S.G. Ungar, J.S. Pearlman, J.A. Mendenhall, D. Reuter, Overview of the earth observing one (eo-1) mission, *IEEE Trans. Geosci. Rem. Sens.* 41 (6) (2003) 1149–1159.
- [3] L. Tarabini Castellani, J.S. Llorente, J.M. Fernández Ibarz, M. Ruiz, A. Mestreau-Garreau, A. Cropp, A. Santovincenzo, Proba-3 mission, *Int. J. Space Sci. Eng.* 5 1 (4) (2013) 349–366.
- [4] G. Krieger, M. Zink, M. Bachmann, B. Bräutigam, D. Schulze, M. Martone, P. Rizzoli, U. Steinbrecher, J.W. Antony, F. De Zan, et al., Tandem-x: a radar interferometer with two formation-flying satellites, *Acta Astronaut.* 89 (2013) 83–98.
- [5] F. Flechtner, P. Morton, M. Watkins, F. Webb, Status of the grace follow-on mission, *Gravity, Geoid and Height Systems*, Springer, 2014, pp. 117–121.
- [6] Y. Ohkami, I. Kawano, Autonomous rendezvous and docking by engineering test satellite vii: a challenge of Japan in guidance, navigation and controlbreakwell memorial lecture, *Acta Astronaut.* 53 (1) (2003) 1–8.
- [7] S. Persson, P. Bodin, E. Gill, J. Jørgensen, Prisma—an autonomous formation flying mission, *ESA Small Satellite Systems and Services Symposium (4S)*, Sardinia, Italy, 2006, pp. 25–29.
- [8] N. Shah, P.C. Calhoun, S.-Y. Park, M. Keidar, Canyval-x: enabling a new class of scientific instruments, *AAS/Solar Physics Division Meeting*, vol. 47, 2016.
- [9] J.-P. Park, S.-Y. Park, Y.B. Song, G.N. Kim, K. Lee, H.J. Oh, J.-C. Yim, E. Lee, S.-H. Hwang, S. Kim, et al., Mission analysis and cubesat design for canyval-x mission, *14th International Conference on Space Operations*, Deajeon, Korea, 2016, p. 2493.
- [10] J.L. Schwartz, M.A. Peck, C.D. Hall, Historical review of air-bearing spacecraft simulators, *J. Guid. Contr. Dynam.* 26 (4) (2003) 513–522.
- [11] T. Rybus, K. Seweryn, Planar air-bearing microgravity simulators: review of applications, existing solutions and design parameters, *Acta Astronaut.* 210 (2016) 239–259.
- [12] D. Scharf, F. Hadaegh, J. Keim, E. Benowitz, P. Lawson, Flight-like ground demonstration of precision formation flying spacecraft, *Proc. SPIE*, vol. 6693, 2007, p. 669307.
- [13] H. Daitz, M. Schlotterer, J. Whidborne, M. Sagliano, Development of a combined attitude and position controller for a satellite simulator, *67th International Astronautical Congress (IAC)*, Guadalajara, Mexico, 2016.
- [14] K. Saulnier, D. Pérez, R. Huang, D. Gallardo, G. Tilton, R. Bevilacqua, A six-degree-of-freedom hardware-in-the-loop simulator for small spacecraft, *Acta Astronaut.* 105 (2) (2014) 444–462.
- [15] P. Tsiotras, Astros: a 5dof experimental platform for research in spacecraft proximity operations, *AAS Guidance and Control Conference*, Breckenridge, Colorado, USA, 2014.
- [16] R. Zappulla II, J. Virgili-Llop, C. Zagaris, H. Park, M. Romano, Dynamic air-bearing hardware-in-the-loop testbed to experimentally evaluate autonomous spacecraft proximity maneuvers, *J. Spacecraft Rockets* 54 (4) (2017) 825–839.
- [17] Y. Eun, C. Park, S.-Y. Park, Design and development of ground-based 5-dof satellite formation flying testbed, *AIAA Modeling and Simulation Technologies Conference*, AIAA SciTech Forum, San Diego, California, USA, 2016.
- [18] Y. Eun, S.-Y. Park, Preliminary experimental results and development status on asterix facility, *9th International Workshop on Satellite Constellations and Formation Flying*, Boulder, Colorado, USA, 2017.
- [19] L. Kaltenegger, M. Fridlund, The Darwin mission: search for extra-solar planets, *Adv. Space Res.* 36 (6) (2005) 1114–1122.
- [20] J. Llorente, A. Agenjo, C. Carrascosa, C. De Noguera, A. Mestreau-Garreau, A. Cropp, A. Santovincenzo, Proba-3: precise formation flying demonstration mission, *Acta Astronaut.* 82 (1) (2013) 38–46.
- [21] J.R. Wertz, W.J. Larson, *Space mission Analysis and Design*, Microcosm Press, El Segundo, CA, 1999.
- [22] X. Jian, B. Gang, Y. QinJun, L. Jun, Design and development of a 5-dof air-bearing spacecraft simulator, *International Asia Conference on Informatics in Control, Automation and Robotics*, 2009. CAR'09, IEEE, 2009, pp. 126–130.
- [23] NaturalPoint, Optitrack, <http://www.naturalpoint.com/optitrack/>.
- [24] G.P. Sutton, O. Biblarz, *Rocket Propulsion Elements*, John Wiley & Sons, 2016.